# Modeling and experimental investigation of bubble entrapment for flow over topography during immersion lithography

Holly B. Burnett[*a], Alex C. Wei[a], Mohamed S. El-Morsi[a], Timothy A. Shedd[a], Gregory F. Nellis[a], Chris Van Peski[b], Andrew Grenville[b,c]
[a]Computational Mechanics Center, University of Wisconsin, 1513 University Ave., Madison, WI 53706;
[b]International SEMATECH, 2706 Montopolis Drive, Austin, TX 78741
[c]Intel Corp.,2200 Mission College Blvd., Santa Clara, CA 95052

## ABSTRACT

In immersion lithography, the air gap that currently exists between the last lens element of the exposure system and the wafer is filled with a liquid that more closely matches the refractive index of the lens. There is a possibility that air bubbles, which represent a refractive index discontinuity, may be present in the liquid within the active exposure region and cause errors in imaging. One potential source of bubble generation is related to the flow of liquid over previously patterned features, or topography, during scanning or filling. This microscale entrainment mechanism is investigated experimentally and analyzed using computational fluid dynamics (CFD) modeling.

The contact angle is a critical parameter that governs the behavior of the contact line and therefore the entrainment of air due to topography; the same topography on a hydrophobic surface is more likely to trap air than on a hydrophilic one. The contact angle can be a strong function of the flow velocity; a hydrophilic surface can exhibit hydrophobic behavior when the velocity of the free surface becomes large. Therefore, the contact angle was experimentally measured under static and dynamic conditions for a number of different surfaces, including resist-coated wafers. Finally, the flow of liquid across 500-nm deep, straight-sidewall spaces of varying width was examined using both experimental visualization and CFD modeling. No air entrainment was observed or predicted over the velocity and contact angle conditions that are relevant to immersion lithography. The sharp-edged features studied here represent an extreme topography relative to the smoother features that are expected on a planarized wafer; therefore, it is not likely that the microscale entrainment of bubbles due to flow over wafer-level topography will be a serious problem in immersion lithography systems.

**Keywords:** Immersion lithography, fluid flow, bubbles, entrainment

## 1. INTRODUCTION

Immersion lithography has been proposed as a potential method of extending optical lithography to sub-100 nm feature sizes[1]. This technology relies on the insertion of a fluid that has a large index of refraction relative to air into the gap between the wafer and the final lens of the exposure tool. The increased index of refraction enables the printing of smaller features by effectively increasing both the numerical aperture and the depth of focus of the lens system. In the initial implementation of immersion lithography using 193-nm illumination, water will be used as the immersion fluid.

A prototypical fluid management system for an immersion tool is illustrated in Fig. 1. The fluid is continuously pumped through dispense ports that are located adjacent to the lens. The water is removed through recover ports that are located outboard of the dispense ports. In this system, fluid passes under the lens due to the wafer motion that is inherent in the scanning process. Note that a water meniscus forms between the lens housing and the wafer; this meniscus is nominally stationary relative to the lens so there is a relative velocity between the meniscus contact line (i.e., the intersection of the meniscus with the wafer) and the wafer as the scanning process occurs. The wafer motion will be oscillatory and characterized by velocities as high as 1 m/s and accelerations as high as two times the acceleration of gravity.

One of the challenges of immersion lithography is the potential existence of bubbles in the fluid. The curved gas/liquid interfaces associated with bubbles and air pockets will reflect and refract the incident light, distorting image patterns and decreasing yield. The relative motion between the contact line and the substrate presents several potential mechanisms for entraining air in the fluid. These include macroscopic mechanisms such as meniscus break-up, film-pulling, and air entrainment, as well as microscopic mechanisms such as flow over wafer topography related to printed features.[2,3] In this paper, the solid-liquid-gas interface is examined; this region is referred to as the three-phase contact line, or the triple line. The angle between the liquid-gas interface and the solid surface in the absence of any relative motion between the two is called the static contact angle, $\theta_S$, illustrated in Fig. 2a.

When the contact line is in motion, the dynamic contact angle, $\theta_D$, is different than the equilibrium static contact angle, as shown in Fig. 2b and 2c. The static contact angle provides a baseline for studying the dynamic contact angle and is a necessary boundary condition for computational fluid dynamics (CFD) simulations. Unlike the dynamic contact angle, the static contact angle is a property of a given liquid/surface pair and can be used to characterize the wetting properties of a given surface. The static contact angle hysteresis, or the difference between the advancing and receding static contact angles, which are discussed in detail below, provides an important measure of the nano- and mirco-scale homogeneity of a surface. Thus, it is important in any study of surface wetting, such as the situations inherent to immersion lithography, to characterize the surface using static contact angles.

The dynamic contact angle can vary from 0º to 180º for a given liquid-solid-gas combination depending on the contact line velocity and the direction of its motion relative to the substrate. This variation alone can lead to the macroscopic entrainment of air at the contact line. Voinov's equation[4] can be used to approximately predict the effect of velocity ($U$, taken to be positive in the advancing case) on the dynamic contact angle:

$$\theta_D^3 = \theta_S^3 + 9\frac{\mu U}{\sigma}\left[\ln\left(\frac{H}{L_S}\right) + C\right] \tag{1}$$

where $H$ is the half-width of the gap (nominally 0.5 mm for immersion lithography), $\mu$ is the viscosity of the fluid, $\sigma$ is the surface tension, and $C$ is a solution constant that is equal to 1.5 for a slot. In Eq. (1), $L_s$ is the slip length, which is related to the inner-scale physics of the meniscus and is typically expressed as $\mu/\beta$, where the slip coefficient, $\beta^{-1}$, has a value of on the order of $3 \times 10^{-4}$ to $10 \times 10^{-4}$ $cm^3$/dyn-s.[4] The exact value of the slip length has a very small effect on the dynamic contact angle. It is noted that Voinov’s equation is strictly valid for vanishingly small Reynolds number flows, whereas a relatively large Reynolds number, on the order of 1000, will characterize the flow conditions expected in immersion lithography. Nevertheless, the correlation provides some understanding regarding the likely impact of substrate motion on the behavior of the meniscus.

Equation (1) contains an important non-dimensional grouping known as the capillary number, Ca,

$$\text{Ca} = \frac{\mu U}{\sigma} \tag{2}$$

This is essentially a ratio of the viscous forces acting on the fluid near the contact line and the surface tension forces acting at the contact line. Since the surface tension is assumed to be constant in this study, Ca can be thought of as a non-dimensional velocity, scaled according to the forces that are significant to the phenomena of interest.

The macroscopic phenomenon referred to as air entrainment on a flat surface occurs when the substrate moves into the meniscus (towards the liquid side, see Fig. 2c) with sufficient velocity so that the dynamic contact angle approaches 180º, at which time air is pulled into the liquid at the substrate surface. Equation (1) indicates that for surfaces with static contact angles ranging from 60º to 120º, the velocity required to produce macroscopic air entrainment of this nature exceeds 17 m/s, which is well above the expected substrate velocity for immersion lithography. However, the flow of the meniscus over micro-scale wafer topography may result in air entrainment through a fundamentally different mechanism, shown in Fig. 3. The contact line may become attached, or pinned, to the edge of a sharp feature, effectively forcing the contact angle towards 180º as the liquid above the attached contact line continues to be pushed forward by the bulk of the flow. The bulk flow may pass over the feature before the meniscus reaches the bottom, leaving an unfilled region in the channel. The filling behavior is dominated by the contact angle; small differences in static contact angle can result in very different behavior. For example, CFD simulations predict that a 1000-nm wide feature that is 500 nm deep will be completely filled if the static contact angle is 60º, but will entrain air if the static contact angle is 75º.[5]

This paper describes both experiments and CFD models that have been developed in order to investigate the microscopic entrainment of air at a moving contact line due to surface topography. The conditions for the topography studies and the boundary conditions for the CFD models are determined through experimental surface characterization of the static and dynamic contact angle on resist-coated wafers using representative wafer velocities. The pathological case of flow over micro-scale, sharp-edged features is investigated experimentally and through CFD simulation. No air

entrainment was either observed or predicted under conditions that are consistent with those expected for immersion lithography.

## 2. STATIC CONTACT ANGLE MEASUREMENTS

### 2.1. Experimental Facility

A schematic of the facility used to measure the static contact angle is shown in Fig. 4a. The test surface (e.g., a resist-coated wafer) is mounted to the platform and the position of the surface can be controlled by horizontal, vertical and rotational translation stages that are affixed to a vibration-isolated optical table. An injection needle is mounted to a second vertical translation stage so that it is perpendicular to the test surface. The dispense process is actuated by a syringe pump that is controlled via a personal computer (PC) through a LabVIEW interface. The syringe pump is used to deposit a precise volume of fluid onto the surface. Images of the droplet are acquired along an axis that is parallel to the test surface using a 1.4 megapixel, digital charge-coupled device (CCD) camera (Model QiCAM, Qimaging, Inc.) that is interfaced with, and controlled by, a PC. The camera has a resolution of 1392 × 1040 pixels and generates a 12-bit digital output. The entire facility is enclosed and can be purged with dry nitrogen or dry air in order to mitigate humidity fluctuations and minimize the number of particles in the test enclosure. The humidity within the enclosure is monitored using a hygrometer, but was found to have no significant effect on the contact angle measurements reported for this study. The drop is illuminated from behind by a 150-W quartz halogen fiber optic light source directed at an opalized glass diffuser.

On an ideal, planar, homogeneous surface, the static contact angle is unique. However, many surfaces exhibit contact angle hysteresis due to physical and/or chemical surface inhomogeneities. A drop on a flat, horizontal surface that is slowly tilted will adopt an asymmetric shape, as shown in Fig. 4b. The leading edge will tend to exhibit a contact angle that is greater than the horizontal static contact angle. The limiting value of this angle, that is, the value just before the drop begins to move, is defined as the advancing static contact angle, ($\theta_A$). Similarly, the trailing edge will tend to exhibit a smaller angle than the horizontal static contact angle. The value of this angle just prior to droplet motion is defined as the receding static contact angle, ($\theta_R$). The difference between the advancing and receding angles is referred

to as the contact angle hysteresis and reflects the degree of heterogeneity of the surface. To characterize the degree of contact angle hysteresis and level of homogeneity associated with a wafer surface, a rotational stage was incorporated into the facility depicted in Fig. 4a.

**2.2. Test Procedure and Analysis Algorithm**

A non-resist coated test surface is prepared for contact angle measurements by cleaning it with a optical surface cleaning solution followed by a methanol wipe. A resist-coated test surface is prepared only by blowing the surface with a dry air nozzle in order to remove particulate contamination. The test surface is then mounted to the platform within the enclosure and a series of images are acquired. For static contact angle measurements, the horizontal translation stage is used to move to an open location on the test surface, then a syringe pump is used to deposit a drop of deionized water through an injection needle at a precise location. The volume of the drops used ranged from 12 to 65 μl, depending on the general hydrophobicity of the surface. For the advancing and receding contact angles, the operator slowly turns the rotating stage control knob, which tilts the platform and test surface. As the surface is tilted, a series of images are acquired along an axis that is parallel to the test surface using the CCD camera. The advancing and receding contact angles are measured using the image that is taken immediately before the drop begins to move. In order to precisely characterize a surface, this process is repeated several times and a series of images is gathered and analyzed.

Images are processed using a custom image processing algorithm developed using commercially available machine-vision automation software. The algorithm uses an edge finding technique to locate the two contact points where the drop meets the surface, as illustrated in Fig. 4b. A secondary edge finding operation is performed along lines that are parallel to the line defined by these two contact points in order to locate two points on the edge of the drop that are 10 pixels (~ 200 μm) from the surface. These points, together with the contact points, define lines that are tangent to the drop at the two drop edges. The angles between horizontal and the tangent lines are measured and recorded as the static contact angle for horizontal surfaces. For drops on a rotated surface, the platform tilt angle is subtracted in order to determine the advancing and receding contact angles.

The dominant sources of error related to the contact angle measurement technique are related to the ability of the image processing algorithm to locate either of the two points that are required for the tangent line calculation. An estimation of the error associated with a single image measurement of the contact angle can be examined by assuming a reasonable error in the position of these points (specified in terms of camera pixels). After artificially shifting the points, the slope of the tangent line is recalculated and the change in the contact angle, relative to the nominally measured value, is taken to be the worst-case error. For a typical image, five pixel shifts in the location of either tangent point will change the measurement by less than ±0.6º; multiple image measurements will improve the uncertainty and at least 30 images are used for a typical static contact angle measurement.

**2.3. Validation and Results**

Static contact angle data were acquired on a number of test surfaces, including resist-coated wafers. The results are summarized in Table 1. The small standard deviation and measurement uncertainty for these measurements shows that the system is capable of making very precise contact angle measurements. The standard deviation is always larger than the theoretical, multiple measurement uncertainty due to surface heterogeneities; recall that each static contact angle measurement is made at a different location on the test surface. It was clear that the image-to-image deviations were in the data and not due to the measurement technique; that is, it was obvious that the contact angle of the droplet did in fact depend on its location on the wafer and the measurement technique was accurately reporting this. Note that the measured contact angle for the 300 mm wafer coated with TOK TSP-3A topcoat treatment is 117.4º ± 0.08º with a standard deviation of 0.44º (the last entry in Table 1). The manufacturer of the topcoat reports a static contact angle of 117º measured with a commercially available optical goniometer.

It is interesting that the hysteresis measurements (i.e., the difference between the advancing and receding contact angles for a given surface) do not strongly correlate with the static contact angle variations. This indicates that the resist-coated wafers have different levels of uniformity on the macroscopic and microscopic scales. The spin-coated wafers are generally macroscopically more uniform than the manually prepared quartz and glass surfaces. However, the large hysteresis numbers suggest that the molecular structure at the resist surfaces is not very uniform.

## 3. DYNAMIC CONTACT ANGLE MEASUREMENTS

### 3.1 Experimental Setup

In order to observe dynamic contact angles under quasi-steady flow conditions, it was necessary to build a test facility with a nominally stationary meniscus that could be imaged continuously as a substrate advanced into it. The key components of such a facility are shown in Fig. 5a. Distilled water is injected manually into a gap between a 25.4 mm diameter window suspended above the substrate. The gap height can be precisely set using a digital micrometer and the window holder can be adjusted so that the window and substrate are parallel. The substrate is mounted to an Aerotech ALS10010 translation stage, which is used to control its velocity, displacement amplitude and acceleration ramp time via a computer interface. The total travel of this stage is 100 mm with a maximum speed of 750 mm/s and 20 m/s$^2$ maximum acceleration.

The substrate is then advanced into the meniscus and a series of side-view images of the meniscus are taken with a digital high-speed camera (IDT, Inc., Model XS3). This CMOS-based camera has a peak resolution of 1280 x 1024 pixels at a frame rate of 650 Hz, with frame rates of up to 32000 Hz possible by acquiring thinner strips of images. Lighting is achieved with two 150-W quartz-halogen fiber optic light sources. One is used to illuminate the meniscus from the front, while the other is aimed at a reflective surface behind the meniscus, providing back-lighting. The frame rate required increased from 100 Hz to 2000 Hz and the shutter speed required decreased from 0.5 ms to 0.05 ms as the peak substrate velocity was increased from 0.01 m/s to 1.0 m/s. As the substrate velocity increases, the frame rate was increased in order to acquire a sufficient data set in the time associated with the limited travel of the motorized linear stage. Blurring will occur at these higher velocities if a short shutter speed is not used. These settings enabled useful data to be extracted from images with minimal light and high shutter speeds, as the sample image in Fig. 5b shows. This test facility also allows acquisition of large data sets, as the meniscus remains in the field of view of the camera at all times.

The sets of images are batch processed using commercial machine vision automation software. First, the image contrast is enhanced by multiplying each pixel value by a constant, ranging from 3 to 12 depending on the brightness of the image (darker images require a higher multiplier). An edge finding tool is then employed to determine the line that is

tangent to the meniscus at the point where it meets the surface. The image multiplier and the contrast settings of the edge finding tool must be adjusted according to image brightness. A digital image processing local averaging filter is sometimes employed to improve contrast for darker images. A 3 x 3 local averaging filter creates a new image by determining each pixel value from an average of the adjacent pixel values in the original image. This also acts to blur any blemishes that might be exaggerated by the multiplier.

The tangent line is defined in a manner that is consistent with both the static contact angle and contact angle hysteresis measurements. The dynamic contact angle is defined as the angle between the substrate surface and the line drawn between the contact point and the point on the meniscus edge 10 pixels (~200 μm) above the surface. Batches of images are processed automatically and the resulting angles are written directly to a spreadsheet file. As the substrate moves into the meniscus at higher velocities, the meniscus may go out of focus due to distortions of the contact line and the images become progressively darker due to the faster shutter speeds. Any data images that are out of focus are rejected.

### 3.2 Results

As a means of effectively bracketing the range of values expected for the resist surfaces, dynamic contact angles were measured on the quartz mask blank and Rain-X treated glass at a gap height of 1 mm and velocities ranging from 0.01 to 1 m/s. The results are shown in Fig. 6. For the range of velocities investigated, the quartz exhibits a large increase in contact angle with increasing velocity from 0.01 m/s to 0.1 m/s and then increases slightly as the velocity increases beyond that point. The dynamic contact angle on the Rain-X-treated glass increases slightly as velocity increases over the entire velocity range, from 0.01 m/s to 1 m/s.

## 4. FLOW OVER STRAIGHT-SIDE WALL TOPOGRAPHY

### 4.1 Experimental Observations

To study the flow over topography in conditions that are relevant to immersion lithography, a fluid dispense and recover system has been constructed. A schematic of the system is shown in Fig. 7 and a photograph is shown in Fig. 8. This system allows experiments to be conducted in which a moving wafer mounted on a motorized stage assembly is dragged under a stationary meniscus at velocities up to 1 m/s.

Fluid can be dispensed at flow rates up to 500 ml/min either through the injection needles, through three dispense ports, or both. A fluid recover ring surrounds the lens region and has four connections to a vacuum line which can provide up to 30 in. Hg vacuum. The dispense/recover assembly is positioned over a moving substrate. The CMOS high speed camera is mounted below the assembly and the meniscus is viewed through the glass substrate, as shown in Fig. 8. The system is supplied with water by a peristaltic pump and a vacuum pump in a continuous closed-loop configuration.

Fig. 9a illustrates an image taken after bubbles have been injected into the fluid. Notice even very small bubbles (down to the smallest bubbles that were present, 7.3 μm in Fig. 9a) are clearly visible. This image verifies the ability of the imaging system to detect air entrainment at the micron scale.

A number of line-space patterns were etched in a quartz substrate; the depth of the grooves were all 0.5 μm whereas the width varied from 1 μm to 2 μm and the pitch varied from 0.6 μm to 10 μm. In terms of the potential for air entrainment, the worst-case pattern on the substrate was the 1 μm wide, 0.5 μm deep lines with 1 μm spacing. Figures 9b and 9c show images of a 600 μm square segment of this pattern just before and immediately after the substrate was pulled under the water meniscus with a velocity of 1.0 m/s. Notice that in Fig. 9c there is no evidence of any air entrainment.

### 3.2. CFD Simulations

The progression of a flow over sharp-edged, vertical-sidewall features with 0.5 μm depth was investigated using CFD modeling via the technique described by Wei et al.[6] As in the experiments detailed above, a contact line velocity of 1 m/s was chosen, since this seems to be an upper bound for contact line motion in immersion lithography systems. As noted above, the advancing dynamic contact angle increases with velocity, so performing the simulation at the upper bound of 1 m/s presents conservative results. Figure 10 illustrates a map of the results presented in the parameter space of feature width and contact angle. The regions in which the feature is completely filled and clearly entrains air are both indicated; note that hydrophobic and deep features tend to entrain air. Also shown are the conditions associated with the various patterns on the test wafer. Note that no air entrainment is predicted by the CFD model for any of the patterns on the substrate, which is consistent with the experimental observation.

Figure 11 shows a comparison between CFD results, experimental results, and numerical predictions of dynamic contact angle plotted with respect to the capillary number, or non-dimensional velocity, Ca. This can be related to the absolute velocities presented in Fig. 6 by multiplying the Ca by $\sigma/\mu$ (= 72 m/s for the assumptions used in the CFD simulation). Although Voinov's equation is only valid for vanishingly small Reynolds number flows, the results show qualitative agreement in the trend.

## 4. CONCLUSIONS

One potential mechanism for the introduction of air into the lens/wafer gap, flow over microscale topography, has been studied here both experimentally and through CFD simulation. The contact angle was identified as a critical input to the entrainment process and therefore it was precisely measured experimentally for the test conditions and surfaces that are relevant to immersion lithography. The flow over a sharp-edged line/space pattern was studied experimentally and via CFD simulations. For the cases studied, air entrainment due to topography was neither observed nor predicted.

## ACKNOWLEDGMENTS

This research was supported by International SEMATECH and DARPA/ARL. Computer support was provided by the Intel Corporation and Microsoft. Special thanks to IMEC for providing sample wafers for testing and verification data. Contact angle data were obtained and processed by undergraduate research assistants Benjamin Spike and Jennifer Downing.

## REFERENCES

1. M. Switkes and M. Rothschild, "Resolution Enhancement of 157 nm Lithography by Liquid Immersion," *Journal of Microlithography, Microfabrication, and Microsystems,* Vol. 1, No. 3, pp. 225-228, 2002.
2. A. Wei, A. Abdo, G. F. Nellis, R. L. Engelstad, and E. G. Lovell, "Predicting Air Entrainment during Filling Process for Immersion Lithography," accepted by the *Journal of Vacuum Science and Technology B,* 2004.
3. D. Gil, T. A. Brunner, C. Fonseca, N. Seong, R. Streefkerk, C. Wagner and M. Stavenga, "Immersion Lithography: New Opportunities for Semiconductor Manufacturing," *The 48th International Conference on Electron, Ion and Photon Beam Technology and Nanofabrication*, San Diego, CA, June 1 - 4, 2004.
4. J. Petrov, R. Sedev, P. Petrov, "Effect of Geometry on Steady Wetting Kinetics and Critical Velocity of Film Entrainment," *Advances in Colloidal and Interface Science*, Vol. 38, pp. 229-269, 1992.
5. A. C. Wei, “Thermofluid simulations for immersion lithography,” Ph.D. Thesis, University of Wisconsin, Madison, 2004.
6. A. Wei, M. El-Morsi, G. Nellis, A. Abdo, and R. Engelstad, "Predicting Air Entrainment due to Topography During the Filling and Scanning Process for Immersion Lithography," to appear in the *Journal of Vacuum Science and Technology B,* 2004.

TABLE 1

Table 1. Static contact angle measurements showing measurement precision.

| Surface | Contact Angle | Standard Deviation | Number of Samples | Hysteresis | Environment |
|---|---|---|---|---|---|
| Quartz mask blank | 41.5º ± 0.7º | 3.7º | 30 | 15.2° | 17% RH (dry air purge) |
| Commercial quartz | 48.6º ± 0.9º | 4.7º | 30 | 16.3° | 20% RH (dry air purge) |
| Float Glass with RainX | 100.6º ± 0.6º | 3.1º | 30 | 6.9° | 18% RH (dry air purge) |
| Sumitomo PAR817 (150 mm wafer) | 67.7º ± 0.7º | 4.4º | 38 | 34.2° | 20% RH (dry air purge) |
| ARCH GAR8105 (150 mm wafer) | 62.5º ± 0.5º | 2.5º | 30 | 42.3° | 22% RH (nitrogen purge) |
| TOK TARF7047 (150 mm wafer) | 68.4º ± 0.3º | 1.6º | 30 | 35.3° | 21% RH (nitrogen purge) |
| JSR 237J (150 mm wafer) | 70.0º ± 0.3º | 1.6º | 30 | 26.6° | 23% RH (nitrogen purge) |
| TOK TARF6111 (300 mm wafer) | 66.8º ± 0.1º | 0.8º | 38 | 22.7° | 52.3% RH (no purge) |
| TOK TSP-3A Topcoat (300 mm wafer) | 117.4º ± 0.1º | 0.4º | 32 | 11.9° | 52.3% RH (no purge) |

## List of Figure Captions

**Figure 1:** Immersion lithography relies on the insertion of a high refractive index liquid in the lens-wafer gap; the motion of the contact lines associated with the liquid/substrate interface over wafer topography may entrain air.

**Figure 2:** Definition of (a) static contact angle, (b) dynamic contact angle for receding fluid and (c) advancing fluid.

**Figure 3:** CFD predictions of the progression of flow at a velocity of 1 m/s over a straight side-wall feature that is 250 nm-wide and 500 nm-deep, illustrating the mechanism by which air may be entrained: (a) flow on the hydrophilic surface approaches the feature, (b) during fill, the apparent contact angle is hydrophobic, (c) bulk of flow reaches opposite edge of feature causing the meniscus to rupture, and therefore (d) a pocket of air is entrained in the feature.

**Figure 4:** (a) Schematic of the static contact angle measurement facility as seen from the point of view of the camera. (b) Sample image illustrating the advancing and receding contact angles on a stationary droplet.

**Figure 5:** (a) Components of the dynamic contact angle measurement facility. (b) Example of a dynamic contact angle data image.

**Figure 6:** Dynamic contact angle results for the quartz mask blank and Rain-X treated float glass

**Figure 7:** (a) Bottom view and (b) side view of the simultaneous fluid dispense and recover system.

**Figure 8:** (a) dispense/recover system with camera and motorized linear stage, and (b) close-up of dispense/recover system

**Figure 9**. (a) Image of water in which air bubbles have been injected, verifying the ability of the imaging system to detect micron-scale air entrainment. The images to the right show a 600-μm square image of the worst-case pattern that consists of 1.0 μm wide lines with depth 0.5 μm on a 1.0 μm pitch, (b) just before and (c) immediately after the substrate was moved under the meniscus. Note that in image (c), the lines are immersed in water and there is no evidence of any air entrainment.

**Figure 10:** CFD results showing the regions in which air is entrained (the no fill region) and in which the features fill (definite fill region) for 0.5 μm deep features in the parameter space of feature width and static contact angle

**Figure 11:** CFD, experimental, and numerical results showing qualitative agreement.

FIGURE 1

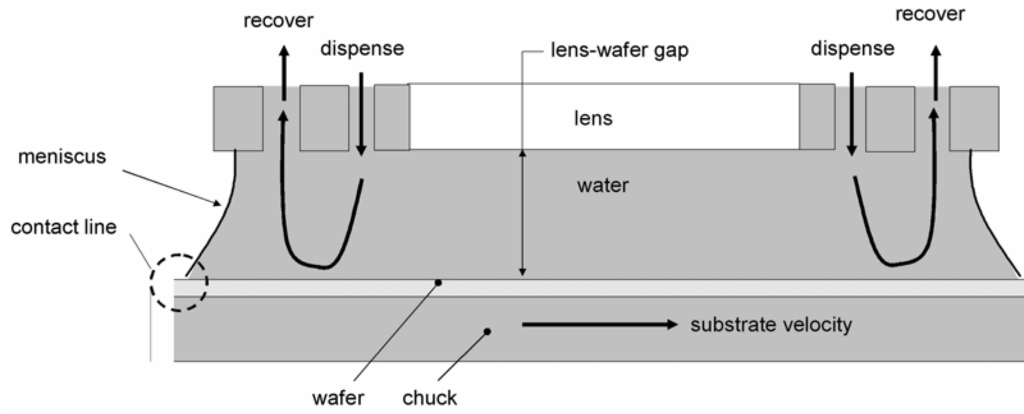


Fig. 1. Immersion lithography relies on the insertion of a high refractive index liquid in the lens-wafer gap; the motion of the contact lines associated with the liquid/substrate interface over wafer topography may entrain air.

FIGURE 2

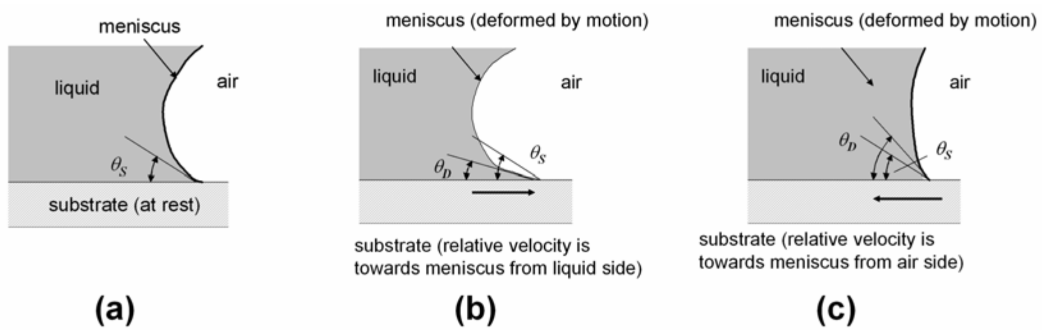


Fig. 2. Definition of (a) static contact angle, (b) dynamic contact angle for receding fluid and (c) advancing fluid.

FIGURE 3

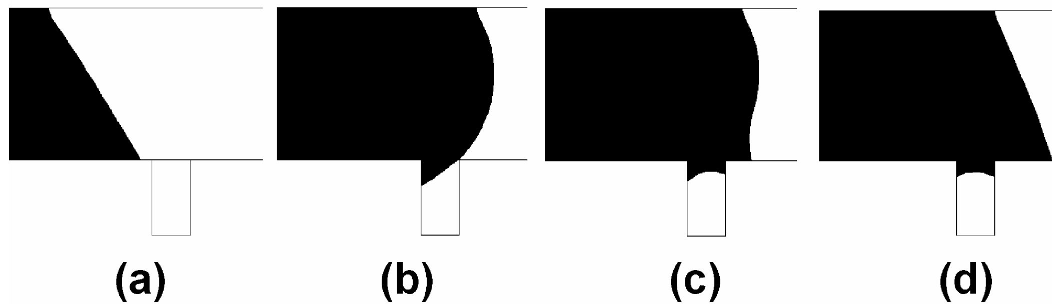


Fig. 3. CFD predictions of the progression of flow at a velocity of 1 m/s over a straight side-wall feature that is 250 nm-wide and 500 nm-deep, illustrating the mechanism by which air may be entrained: (a) flow on the hydrophilic surface approaches the feature, (b) during fill, the apparent contact angle is hydrophobic, (c) bulk of flow reaches opposite edge of feature causing the meniscus to rupture, and therefore (d) a pocket of air is entrained in the feature.

FIGURE 4

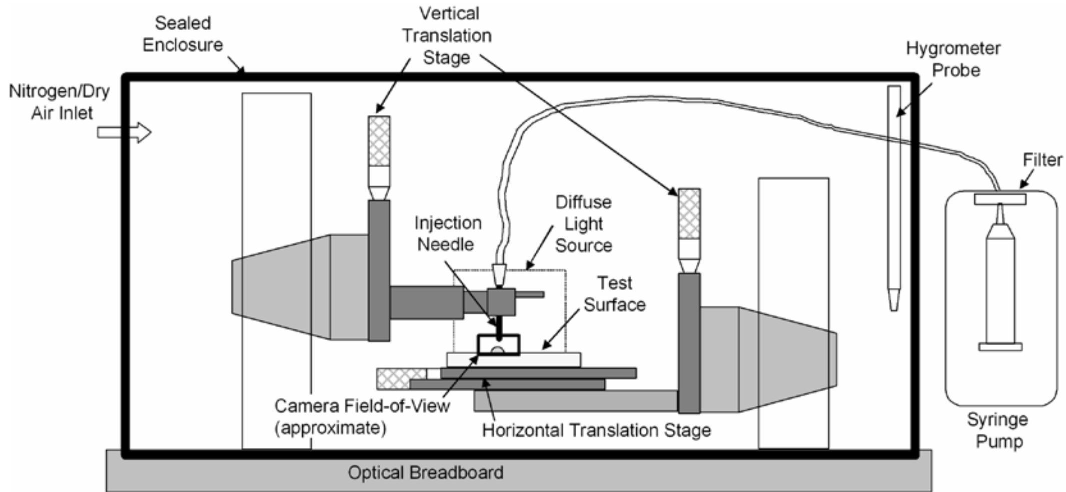


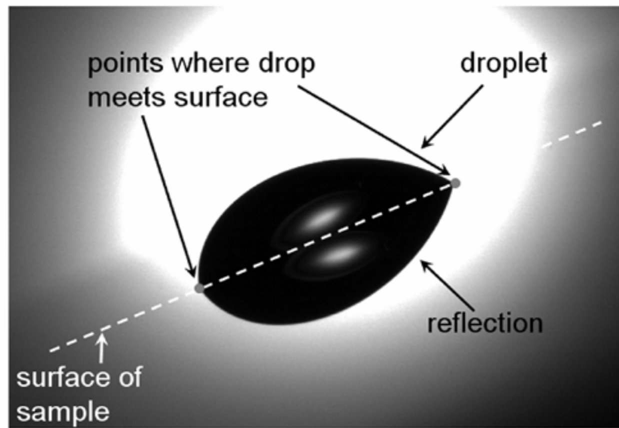


(b)

Fig. 4. (a) Schematic of the static contact angle measurement facility as seen from the point of view of the camera. (b) Sample image illustrating the advancing and receding contact angles on a stationary droplet.

FIGURE 5

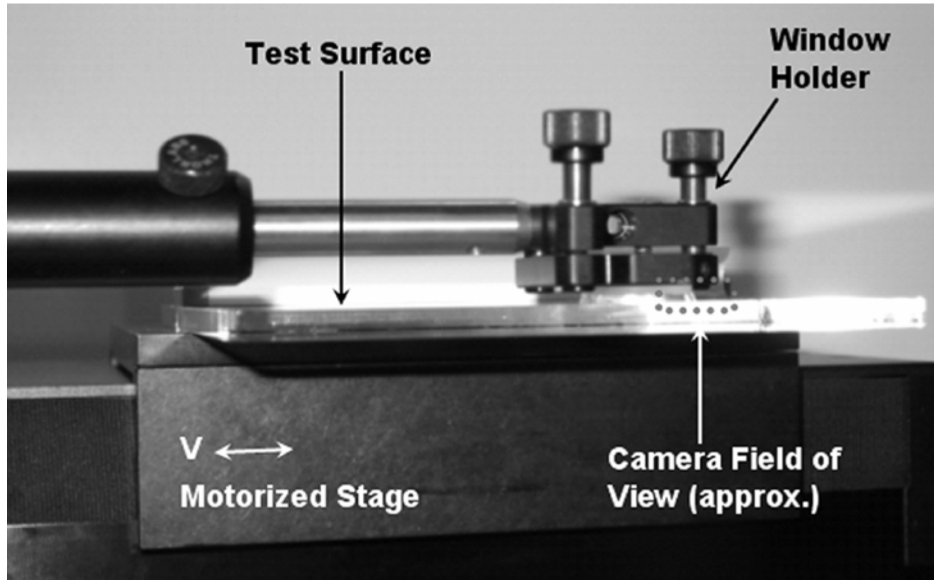


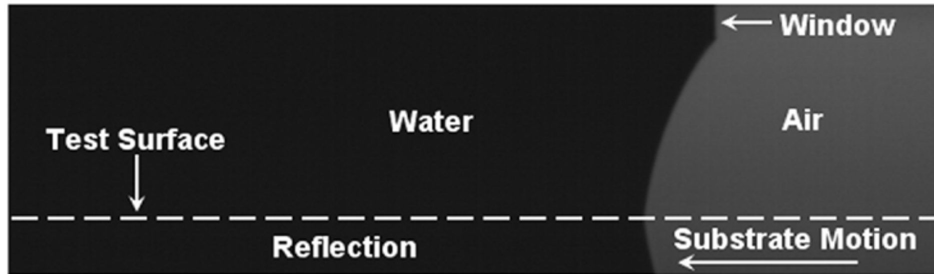


Fig. 5: (a) Components of the dynamic contact angle measurement facility. (b) Example of a dynamic contact angle data image.

FIGURE 6

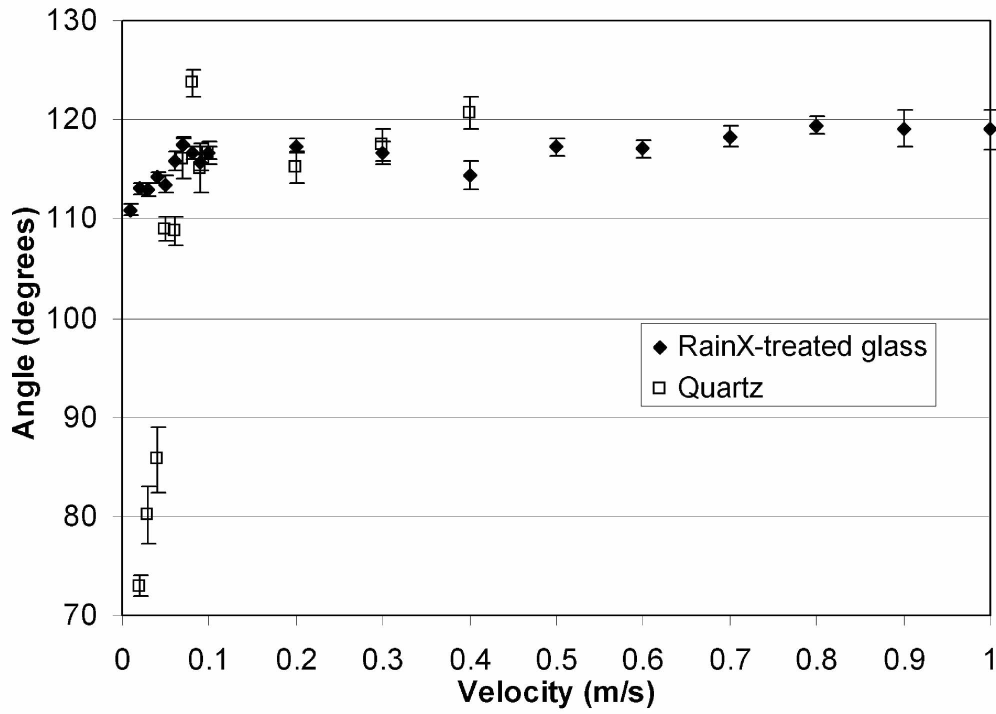


Fig. 6: Dynamic contact angle results for the quartz mask blank and Rain-X treated float glass.

FIGURE 7

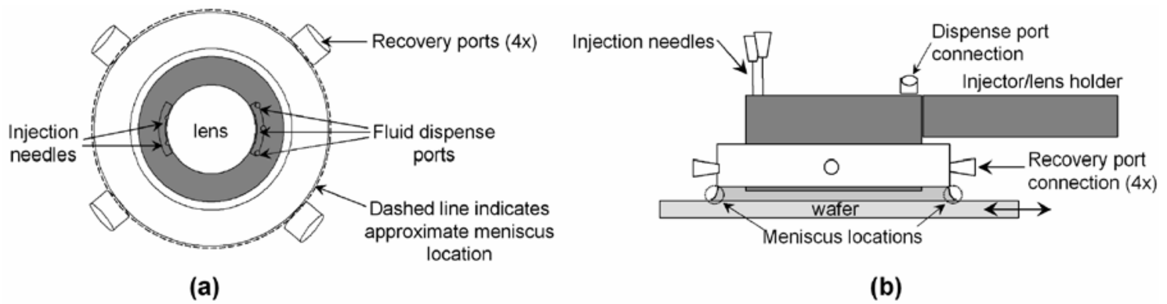


Fig. 7. (a) Bottom view and (b) side view of the simultaneous fluid dispense and recover system.

FIGURE 8

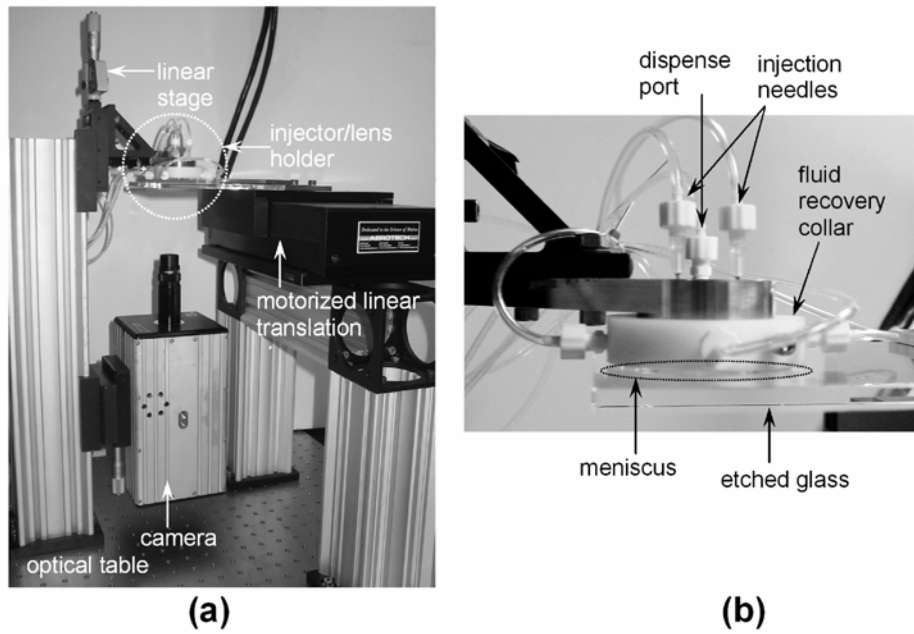


Fig. 8. (a) dispense/recover system with camera and motorized linear stage, and (b) close-up of dispense/recover system.

FIGURE 9

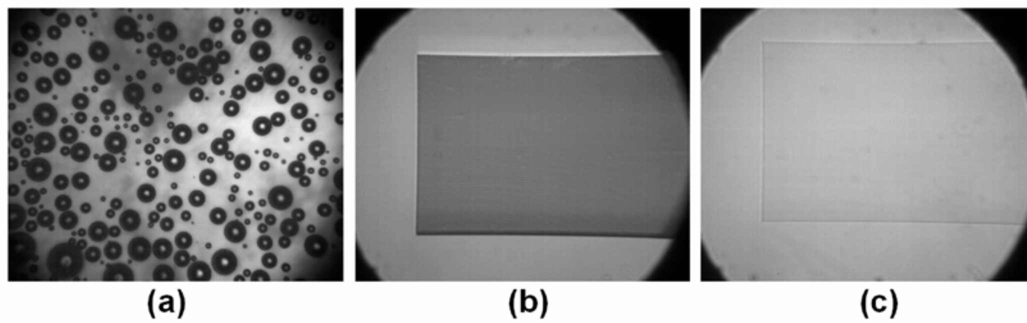


Fig. 9. (a) Image of water in which air bubbles have been injected, verifying the ability of the imaging system to detect micron-scale air entrainment. The images to the right show a 600-μm square image of the worst-case pattern that consists of 1.0 μm wide lines with depth 0.5 μm on a 1.0 μm pitch, (b) just before and (c) immediately after the substrate was moved under the meniscus. Note that in image (c), the lines are immersed in water and there is no evidence of any air entrainment.

FIGURE 10

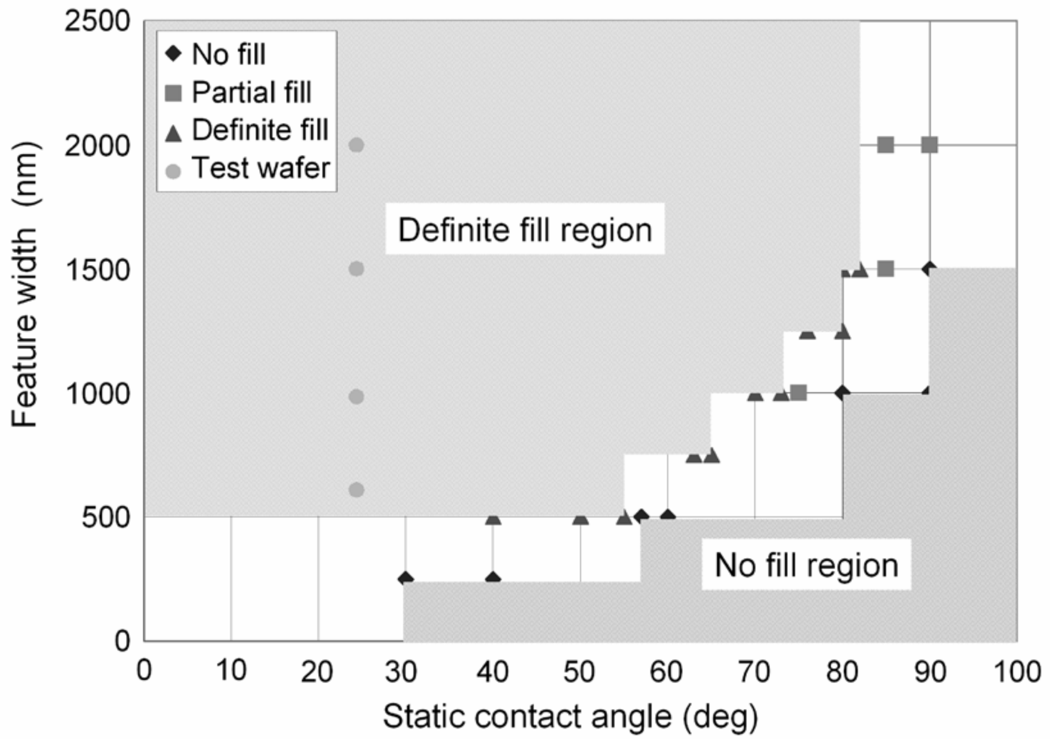


Fig. 10. CFD results showing the regions in which air is entrained (the no fill region) and in which the features fill (definite fill region) for 0.5 μm deep features in the parameter space of feature width and static contact angle.

FIGURE 11

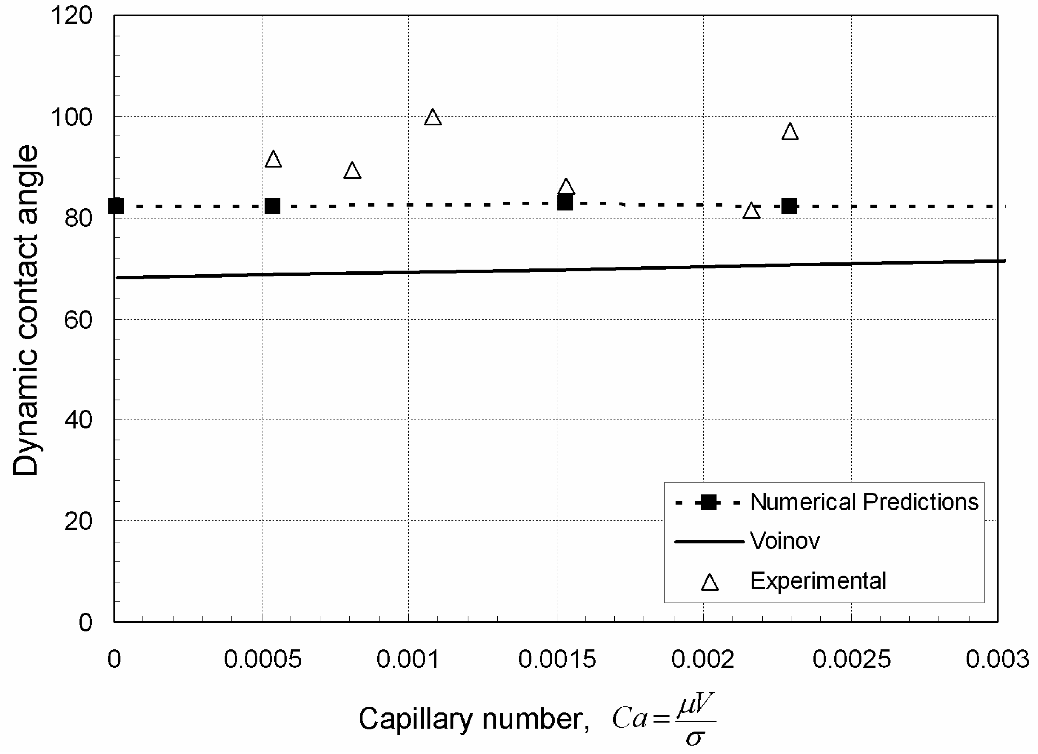


Fig. 11. CFD, experimental, and numerical results showing qualitative agreement.